ELSEVIER

Ceramics International 26 (2000) 807–819

CERAMICS INTERNATIONAL

Role of fabrication route and sintering on wear and mechanical properties of liquid-phase-sintered alumina

Amiya P. Goswami [a,*], Gopes C. Das [b]

[a] *Ceramic Technological Institute, Bharat Heavy Electricals Limited, Bangalore 560 012, India*
[b] *Department of Metallurgical Engineering, Jadavpur University, Calcutta 700 032, India*

Received 10 October 1999; received in revised form 2 November 1999; accepted 22 February 2000

Abstract

Liquid-phase-sintered Al_2O_3 (LPS) fabricated by slip casting, tape casting, isopressing, uniaxial pressing, piston and auger extrusion showed substantial differences in wear due to differences in morphology as observed in image analyses of SEM micrographs. The abrasive wear was low in the case of uniaxial pressing and high in the case of tape casting in the 'dry sand and rubber wheel' test. The wear surface of the tape cast specimen exhibited extensive microcracking possibly due to orientation of Al_2O_3 platelet (major face) parallel to the abraded surface whereas some degree of perpendicular orientation in extruded surface resulted in lower wear loss. In wet-milling wear test, the isopressed balls of a 95–97 wt% LPS derived from reactive powder (< 1 μm) showed 25% lower wear loss than that of the extruded balls of a 91–94 wt% LPS derived from coarse powder (70–100 μm). Sintering at a lower temperature with longer duration and batch milling of the composition in between 12 and 16 h resulted in low wear loss. Flexural strength also improved by longer sintering time but did not show any improvement by increasing milling time. However, the variation in flexural strength was minimized by isopressing the extruded specimen. A high indentation fracture toughness at 49.03 N test load was associated with (i) large elongated reinforcement grains in a fine-grained microstructure with overall elongated morphology and (ii) with an intergranular fracture.

Keywords: Alumina; Sintering; Wear and mechanical properties

1. Introduction

Fabrication routes like powder compaction by uniaxial or isostatic pressing, extrusion by piston and screw auger, slip casting and tape casting are well known shaping and forming methods in ceramics [1–2]. During fabrication, particles tend to orient in a preferred direction [3–5]. The fabrication route may also influence the properties of the sintered material. For instance, an extruded 95% Al_2O_3 was found to be stronger than materials produced by powder pressing or slip casting [6]. The fracture toughness (Chevron notched) was found to be higher in a certain direction of the extruded specimen when compared to the isopressed specimen [7]. Carisay et al. [8] investigated the mechanical properties of Al_2O_3 platelets oriented by a tape casting process. The alignment of the platelets yielded an increase of 15–25% in the bend strength in the through-thickness direction.

The manufacturing goal in ceramics is to enhance flaw tolerance. Flaw tolerance in nontransforming ceramics like Al_2O_3 and Si_3N_4 can be enhanced [9] by introducing large reinforcement grains in the microstructure. Recently high fracture toughness was reported in self-reinforced Si_3N_4 composite fabricated by tape casting where grains were aligned and grown in a desired manner [10]. Fabrication principle [11] should therefore form an integral part of the microstructural design for mechanically strong and wear resistant ceramics.

Microstructural investigations in alumina ceramics have so far been focussed on the role of cation impurities [12–15]. Cations e.g. Na and Ca are known to trigger discontinuous grain growth [16] in certain preferred crystallographic direction of α-Al_2O_3, while Mg acts as grain growth inhibitor. Therefore, the distribution of the cations in the grain boundary region may determine the grain size and shape in the sintered Al_2O_3 ceramics. Besides, the initial particle size distribution in

* Corresponding author. Presently in Jaya Shree Insulators, Rishra 712 248, India. Fax: +91-33-6722705.
E-mail address: apgoswami@vsnl.com (Amiya P. Goswami).

0272-8842/00/$20.00
PII: S0272-8842(00)00022-5

the starting powder can also influence the microstructure of sintered Al_2O_3 ceramics. Barringer and Bowen [17] addressed the role of starting particle size on the microstructural evolution of the sintered polycrystalline Al_2O_3. They also described the economic implication associated with high purity and monosized submicron powders.

Most commercial powders are usually associated with a relatively higher level of impurities and a wide range of particle size distribution [18]. Characteristics of the initial powder and sintering additives can also influence the final microstructure in the sintered material. Our previous results [19] showed that grain size and shape are influenced by the MgO/(CaO + BaO + KNaO) ratio and SiO_2 content in the chemical composition of 91–94 wt% liquid-phase-sintered Al_2O_3 derived from coarse (70–100 μm) and medium size (3.6–7.0 μm) powders. When MgO/(CaO + BaO + KNaO) ratio was less than 1.0 (A-type materials in our studies), more of elongated large grains were seen in the microstructure. Higher MgO/(CaO + BaO + KNaO) ratio in between 1.0–1.5 (B-type) and 1.5–2.0 (C-type) resulted in equiaxed grains. All these changes were found in the uniaxially pressed specimens sintered isothermally at 1580°C for 2 h.

In the present study, the effect of different fabrication route, sintering temperature/time and certain process parameters such as milling time etc. on grain size, grain shape and orientation pattern in the microstructure has been investigated in 91–94 wt% LPS materials. The mechanical properties like flexural strength, elastic modulus, fracture toughness and wear loss of these LPS materials have been characterized and correlated with the microstructure. A comparison of the wear loss between the isopressed and extruded balls for 91–97 wt% LPS Al_2O_3 will also be presented.

2. Experimental

2.1. Specimen preparation

Different LPS materials were prepared using four kinds of Al_2O_3 powders with different particle size distribution. In the coarse variety, there were two grades ('M' and 'S'), likewise in the medium variety, 'I' grade and in the reactive variety, 'R' (< 1.0 μm) from different sources. A variety of plastic clay (Bikaner clay, India) with known chemical composition and analytical grade chemicals of $CaCO_3$, $BaCO_3$ and MgO were added in the compositions as sintering additives. 91–94 wt% LPS materials have been named as A, B and C based on the MgO/(CaO + BaO + KNaO) ratio. For identification, a suffix has been assigned to each of the compositions, which denotes the grade of the powder used in that composition. The digits after the suffix indicate the milling time (h). The digit before the suffix indicates the serial number of the composition in the increasing order of the MgO/(CaO + BaO + KNaO) ratio. An LPS of 95–97 wt% Al_2O_3 with MgO/(CaO + BaO + KNaO) ratio of 1.87 ($H3_R16$) is also considered for comparison of the results. Many of the details regarding the characteristics of the Al_2O_3 powders, source, chemical composition, material preparation, test procedure and microstructural details of uniaxially pressed specimen have been discussed previously [19–21] and a short summary only will be given here.

All the compositions were wet-milled for 16 h in an alumina bowl using deionised water and Al_2O_3 (~96% Al_2O_3) grinding media. The milling time was specially varied between 4 and 40 h for $A2_M$, $A3_I$ and $A6_M$ materials. The particle size distribution and average particle size (d_{50}) of the milled suspension was measured by X-ray sedimentation (Micromeritics Sedigraph, Model 5100).

The slip was oven dried, pulverized and mixed with an aqueous solution of polyvinyl chloride (~1.5%) as binder for powder compaction. Blocks of 75×25×4 mm size were compacted by uniaxial pressing at ~30 MPa pressure. Balls of about 20 mm diameter were isopressed at ~1000 MPa pressure using an isostatic press (ABB-Autoclave Engineers, USA). The pulverized powder was mixed with 0.25% of methylcellulose and an aqueous solution of polyvinyl chloride (2%) for plastic forming in a de-airing (95% vacuum) pug mill (100 mm barrel dia) fitted with a screw auger [1] for kneading. A solid cylindrical blank was extruded and subsequently machined in dry condition to form balls in the size of ~20 mm diameter. Test rods for flexural strength and modulus of elasticity tests were extruded in 7 and 12 mm diameter, respectively, by the auger extruder. Some of the extruded rods of 7 mm diameter were isopressed at ~400 MPa pressure. All the specimens were oven dried at 110°C and sintered in air (atmospheric pressure) at a peak temperature of 1580±5°C for 2 h except for $C6_R$ which was sintered at 1560°C for 2 h. The cooling rate was 300°C/h maximum.

One of the LPS compositions, which had earlier shown higher wear resistance in our previous study [21], $C2_S$, was used for conducting further experiments on the fabrication route, milling time and sintering temperature/time. A part of the slip was cast after milling in a 'plaster of Paris' mould at a specific gravity of 1.56 and a pH of ~8. Blocks of 60×30×4 mm size were prepared by isopressing at 1400 MPa pressure in a rubber mould. Piston extrusion was carried out in a 150 mm dia (barrel) hydraulic extruder (Wahlco, USA) at 2 MPa pressure at 10 mm/s extrusion speed. In both the piston (hydraulic) and the auger extruders the same plastic mass, prepared as described above was used. Solid blanks of 60×30 mm cross-section were extruded using the same extrusion die at 95% evacuation level. Blanks were sliced with ~4 mm thickness perpendicular to the

extrusion axis. The test surface of the extruded specimens, thus, became perpendicular to the direction of extrusion. The tape casting was done using the Doctor Blade technique [1] with non-aqueous solvents (a mixture of toluene and butanol) and a viscosity of ~900 cps was maintained.

2.2. Characterisation of the sintered specimens

Open porosity and bulk density were measured by the water displacement method [22] as per Archimedes principle. Specimens for microstructural evaluation, hardness and indentation fracture toughness were cut from the bulk of the material. Surfaces perpendicular to the extrusion axis (except in $B6_I16$ where it was parallel) and parallel to the plane of the tape were used for these investigations after polishing progressively with a fine diamond (1 μm) paste. Microstructural characterization was done using an optical microscope (Leitz-Wild Photomat) and a scanning electron microscope (Jeol-JSM 5200) after etching the polished specimen either with boiling H_3PO_4 for ~4 min or by thermal etching at 1370°C for 2 h. An image analyzer with Sigma Scanpro software was employed for measurements of the major axis, minor axis and Feret's diameter of the grains from SEM images. If the ratio between the average major axis and the average minor axis (aspect ratio) was less than 2.1, the microstructure is called equiaxed in our studies and at a higher ratio (>2.1) elongated. The grain size distribution was determined by the 'point count method' on optical micrographs of selected materials. The average grain size calculated from the measurements of the 'point count method' showed a higher value than the software measurement of Feret's diameter.

Vickers hardness (H_v), true hardness (H_0) and fracture toughness were determined by indentations at different loads. The procedure was described in our previous work [20]. Indentation fracture toughness, $K_{ic-short}$, was obtained from the following formula

$$K_{ic-short} = 0.018(E/H_v)^{1/2}P/c^{3/2}$$

where c is the crack length as defined in [23]. True hardness was used in place of Vickers hardness for the calculation of $K_{ic-short}$ in all the $C2_S$ materials that were processed differently. Fracture toughness was also evaluated by the 'single edge notched beam' (SENB) method for a comparison. Flexural strength and elastic modulus (E) were measured by three-point bend test and sonic method respectively [20].

2.3. Wear tests

2.3.1. Abrasion and erosion wear tests

Abrasion tests were conducted on the sintered specimen blocks using dry silica sand abrasive (AFS50) in a 'dry sand and rubber wheel' apparatus described in an ASTM standard [24]. Erosion tests were conducted in a 'dry sand in air jet' test-rig [25] using dry sand abrasive (AFS60). The fired surface was tested and the surface roughness was in the range of 0.7–1.6 μm (Ra-value). Specimen blocks were ultrasonically cleaned, oven dried at 110°C, cooled in a desiccator and then accurately weighed using a high precision digital balance. After the test, the specimen was once again thoroughly cleaned before weighing. The wear volume loss was calculated from the measured mass loss divided by the density of the specimen.

The test conditions in the 'dry sand and rubber wheel' test were as follows: rubber wheel speed, 200 rev. min^{-1}; test duration, 6000 revolutions of the rubber wheel; load on the specimen, 13 kg and sand flow rate, 220–225 g/min. The reliability of the test results was ensured by controlling the test conditions such as nozzle position, sand flow rate, rubber wheel diameter and rubber hardness. A minimum of five tests was run for each sample and the tests were carried out in random sequence. The coefficient of variation in the multiple tests was less than 14%.

In the jet erosion test, dry silica sand stored in a pressure vessel was carried by compressed air and the blast of the jet was made to impinge through a ceramic nozzle of 5 mm diameter on to the test specimen. The velocity of the particles (30 m/s) was determined using a double-disc device and the measurement was made by the ''time of flight'' principle [25]. The test duration was 30 s. The test conditions such as nozzle diameter, abrasive mass flux rate (700 g/min), distance from the specimen to the nozzle and gas pressure were carefully controlled such that the coefficient of variation in the multiple tests was within 15%. The reliability of the test was ensured by testing a standard reference sample prior to actual test and also by the taking average of a minimum three test run on each sample.

2.3.2. Wet-milling test

The wet-milling tests were carried out in a pot mill using Al_2O_3 (AFS90) as abrasives in aqueous media. Four balls from each of the experimental material were used for the test. The test specimens, abrasives and high Al_2O_3 grinding media were charged together into a pot mill along with deionised water and run for 20 h. Both extruded and isopressed balls were tested together in the same run. Test specimens were ultrasonically cleaned before and after the tests, dried in an oven at 110°C, cooled down in a desiccator to ambient temperature and weighed accurately. The surface area of the balls was calculated from the actual measured diameter. The 'mass loss' divided by the 'surface area' of the balls was employed to represent the wear. Average of three test runs was taken and the coefficient of variation in the multiple tests was observed to be within 10%.

After conducting the wear tests, the wear surface was examined in the SEM.

3. Results

3.1. Particle size reduction in batch milling of LPS composition

A plot (Fig. 1) of cumulative mass percentage of finer particles and the corresponding equivalent spherical diameter shows the reduction of particles with the increase in milling time for a typical 91–94 wt% composition ($A2_M$) with coarse Al_2O_3 powder. It shows that the reduction of particle size occurs faster during the initial period of milling and 70–100 μm sized hard agglomerates in the starting powder have reduced to less than 30 μm by 8 h of milling. Milling in subsequent periods resulted in a small change of the d_{50} value i.e. from 2.15 μm after 8 h to 1.80 μm after 16 h. Similarly, the d_{50} value after 4 h of milling is 3.71 μm and that after 12 h is 3.11 μm in $A3_I$ (medium powder). However, the milling time has a significant influence on the distribution of the particle size. In the case of the $C2_S$ composition, a broad particle size distribution is seen after 14 h of milling whereas a narrow distribution is seen after 16 h of milling as shown in Fig. 2. The agglomeration in the milled powder is hardly observed in the SEM images of the green compact.

3.2. Sintering and densification

The effect of milling time on the sintered density and open porosity of uniaxially pressed LPS materials e.g. $A2_M$, $A3_I$ and $A6_M$ is shown in Table 1. It is observed that an increased milling time can yield a high sintered density i.e. 3.73 g/cc for 40 h of milling time for $A6_M$. Table 2 shows the effect of sintering temperature/time on the uniaxially pressed $C2_S$ composition prepared by 14 h and 16 h of milling. Although the small variation (2 h) in the milling time is seen to have no distinguishable effect on the sintered density, an increase in the sintering time has shown some improvement in the sintered density.

A higher green density (2.31–2.37 g/cc) is noticed in isopressed $C2_S14$ compared to that of uniaxial pressed samples (2.06–2.10 g/cc). Table 3 shows the effect of the fabrication route on sintering and densification. Isopressed $C2_S14$ is seen to densify at a lower sintering temperature and in a shorter time (1570°C/1 h) possibly due to a higher green density. On the other hand, a higher sintering temperature/time (1610°C/2 h) is required in the case of slip cast and tape cast materials in order to attain a similar order of open porosity. Extruded specimens have been densified by an increased sintering time (2 h). A further rise in the sintering temperature/time has not shown any significant improvement in density.

3.3. Microstructure in the sintered material

The optical micrographs in Fig. 3(a and b) for $A2_M16$ and that of the $B7_I16$ in Fig. 4(a and b), respectively,

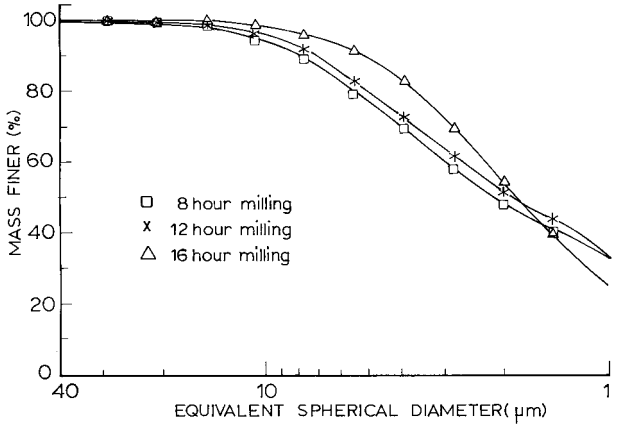

Fig. 1. Particle size distribution (Sedigraph) of $A2_M$ material for different milling time.

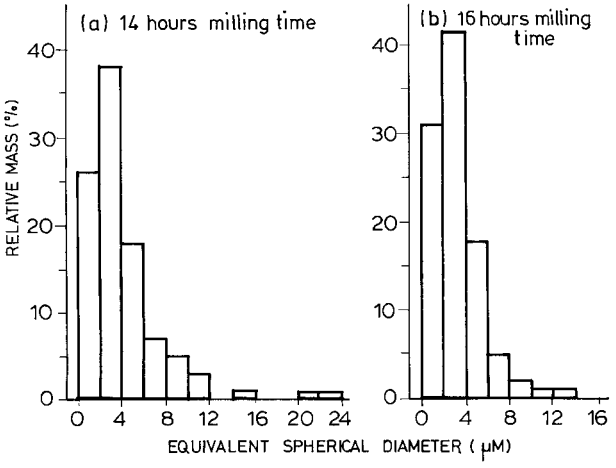

Fig. 2. Histogram showing the particle size distribution for (a) 14 h and (b) 16 h of milling in the $C2_S$ material.

Table 1
Effect of milling time on sintering and wear loss of certain LPS materials

Properties	$A2_M$			$A3_I$		$A6_M$	
	8 h	12 h	16 h	4 h	12 h	16 h	40 h
Sintered density[a], g/cc	3.63	3.53	3.64	3.50	3.52	3.66	3.73
Open porosity[a], %	0.10	0.05	0.10	0.26	0.50	0.18	0.04
Abrasion loss, mm^3	11.38	7.29	5.10	15.02	6.86	3.96	–
Erosion loss at 45°, mm^3	2.83	2.08	2.39	4.92	2.78	1.89	2.58
Erosion loss at 90°, mm^3	3.38	2.65	3.87	5.41	3.95	2.13	4.19

[a] Uniaxial powder pressing.

Table 2
Properties of $C2_S$ materials and wear loss with different milling time and sintering conditions

	(i)	(ii)	(v)	(vi)	(vii)
Milling time, h	14	14	16	16	14
Firing temperature, °C	1570	1600	1570	1600	1570
Soak at peak temperature, h	1	1	1	1	2
Density[a], g/cc	3.48	3.48	3.43	3.49	3.52
Open porosity[a] (%)	0.18	0.12	0.02	0.00	0.00
True hardness, H_0, (GPa)	10.1	11.2	–	9.95	–
Flexural strength $\bar{x}$ (MPa) (σ_{n-1})	275 (43.2)	315 (34.0)	–	189 (39.4)	318 (42.1)
Modulus of elasticity $\bar{x}$ (GPa) (σ_{n-1})	271 (2.3)	272 (5.3)	–	273 (4.6)	–
Abrasion loss (mm^3)	3.14	3.03	3.20	4.35	1.41
Erosion loss at 45°, (mm^3)	1.61	–	–	1.12	–

[a] Powder compaction by uniaxial pressing.

Table 3
The effect of fabrication route on sintering and wear of $C2_S14$ material

	Bulk density g/cc	Open porosity %	Theoretical density %	Vol. loss in abrasion test mm^3
A.1570°C/1 h				
Isopressing	3.53	0.05	92.09	5.29
Extrusion/screw	3.45	0.05	89.90	3.36
Extrusion/ram	3.39	0.09	88.33	3.72
Tape casting	3.50	0.56	91.20	11.66
Slip casting	3.37	0.65	87.92	11.77
B.1570°C/2 h				
Extrusion/screw	3.55	0.00	92.63	3.57
Extrusion/ram	3.50	0.03	91.30	2.66
C.1610°C/2 h				
Tape casting	3.57	0.01	92.97	6.01
Slip casting	3.51	0.06	91.44	3.42

illustrate the change in the grain shape between the uniaxial pressing and auger extrusion. Morphological analysis of the microstructure of sintered (1580°C/2 h) uniaxially pressed LPS were reported in our previous study [19]. It showed that $A2_M16$ had an elongated morphology with an over all aspect ratio of 2.2 and an equiaxed morphology in $B7_I16$ with an aspect ratio of 2.0. The elongation in the extruded specimens of both the materials, however, showed an increasing trend in the aspect ratio in both $A2_M16$ (2.3) and $B7_I16$ (2.2). The two-dimensional observation of the morphology for these materials will be discussed in the subsequent sections.

The micrograph of isopressed $B6_I16$ in Fig. 5(a) shows the dominance of elongated grains with some larger grains 18–24 μm in length and aspect ratio of ~4. The uniaxially pressed specimen of the same material [Fig. 5(b)] also shows the presence of large grains in similar size and shape as that of the isopressed specimens, but the matrix grains are finer and equiaxed (~2 μm). On the other hand, the auger extruded specimen [Fig. 5(c)] has 12–16 μm sized large grains (additionally see the micrographs in Ref. 21). The dimensions and aspect ratios of the large grains were measured directly

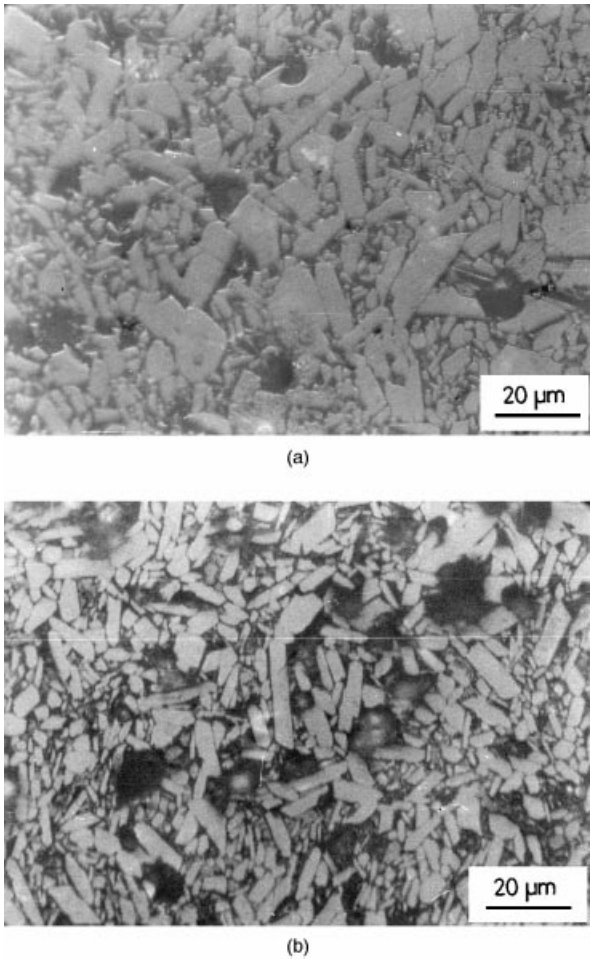

Fig. 3. Optical micrographs (thermally etched) of $A2_M16$ fabricated by (a) uniaxial pressing and (b) auger extrusion in isothermal sintering.

in the optical microscope. The isopressed specimens of $A6_M16$ has a relatively fine microstructure similar to that of the auger extruded $B6_I16$ and the extruded specimen of $A6_M16$ has a microstructure similar to that of the isopressed $B6_I16$. The above observations suggest that the grain size and shape can change with the fabrication route during isothermal sintering.

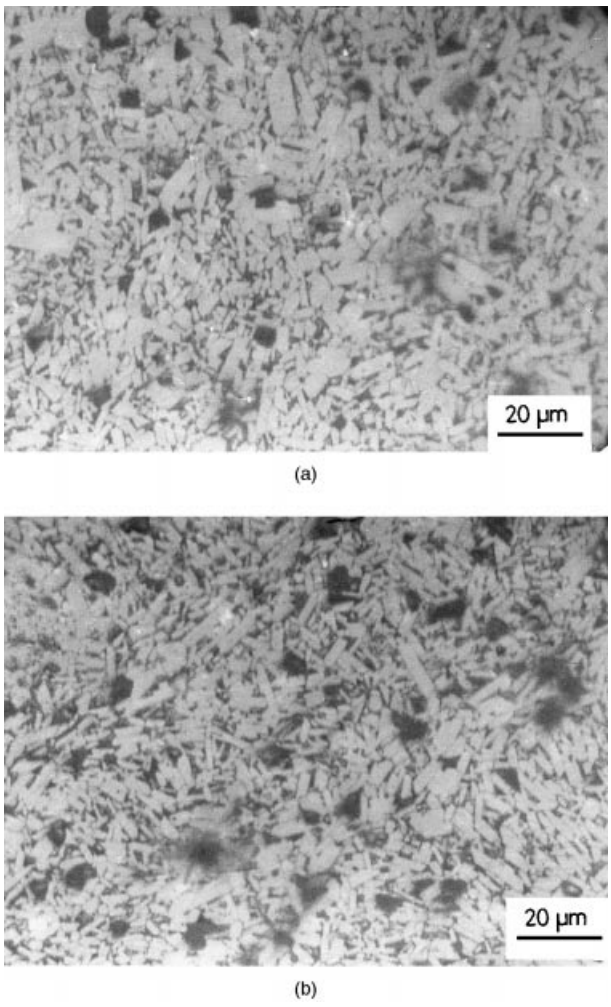

Fig. 4. Optical micrographs (thermally etched) of $B7_I16$ fabricated by (a) uniaxial pressing and (b) auger extrusion showing the difference in morphology after isothermal sintering.

A comparison of the micrographs in Fig. 5(a and b) with that of the Fig. 5(c) suggests a possible orientation of the major face of certain platelets in a plane parallel to the extrusion direction. It may be noted that a similar feature is not detected in Figs. 3(b) and 4(b) because of a different plane of the specimen surface (refer to Section 2.2) examined. Moreover, the movement of the worm in the pug mill may have destroyed the planar alignment of platelets at least partially. As such, the platelet orientation in the screw pattern can hardly be detected in micrographs of sintered auger-extruded specimens (compare figures in 3, 4 and 5).

SEM images of $C2_Si14$ material pressed uniaxially and sintered at 1570°C/1 h [Fig. 6(a)] shows that the grains are predominantly elongated and finer (aspect ratio of 2.3 and Feret's diameter of 2.5 μm). When the sintering temperature is increased ($C2_Sii14$ in Table 2) to 1600°C/1 h, grains are observed to be equiaxed and coarser (overall aspect ratio of 1.9 and Feret's diameter of 3.0 μm) as seen in Fig. 6(b). The SEM image in Fig.

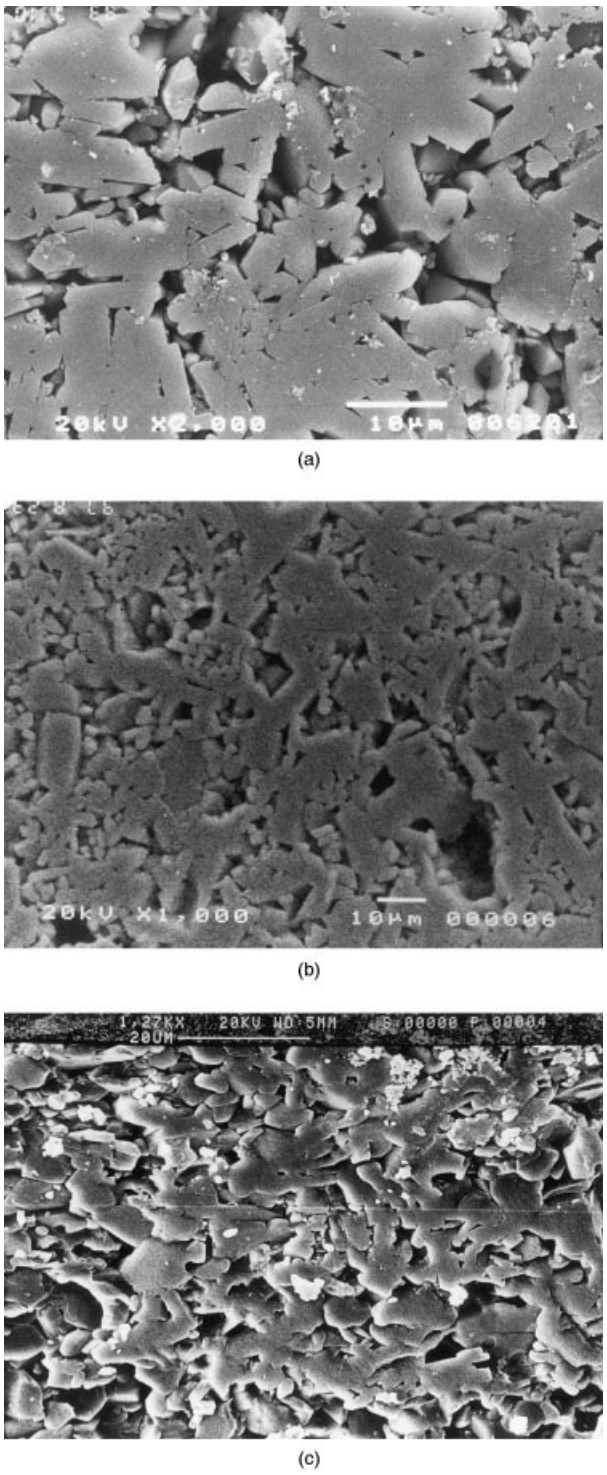

Fig. 5. Chemically etched micrographs of (a) the isostatically pressed ball, (b) the uniaxially pressed block and (c) the extruded-machined ball showing the differences in grain shape and size after isothermal sintering of the $B6_I16$ material.

7(a) for the tape cast specimen of the same material shows an alignment of the major face in the microstructure, whereas a random orientation is observed in the slip cast specimen as seen in Fig. 7(b). Both the tape cast (Feret's diameter of 4.5 μm and aspect ratio of 1.8)

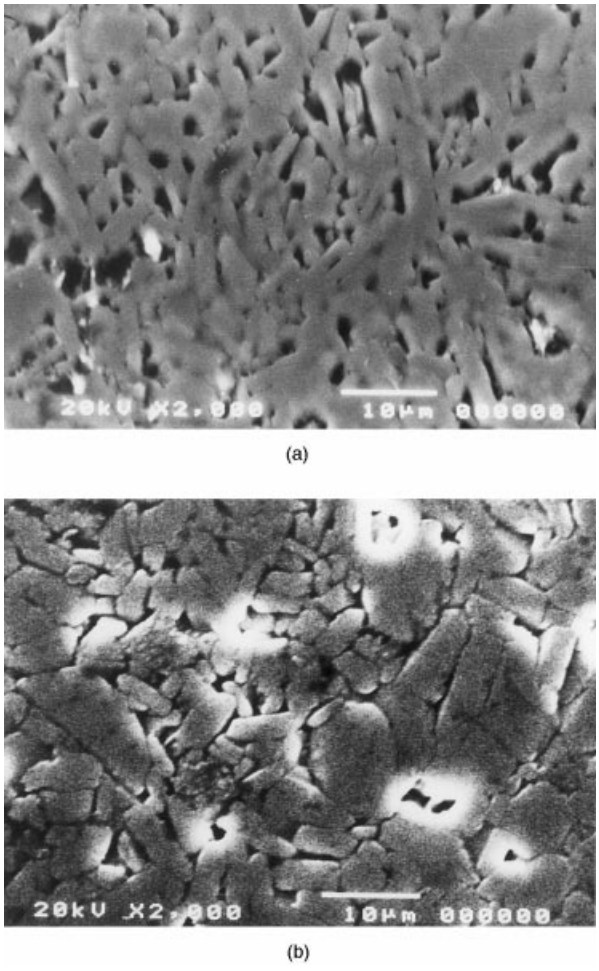

Fig. 6. Back scattered electron images showing the differences in morphology of thermally etched $C2_S14$ materials sintered at (a) 1570°C and (b) at 1600°C both for 1 h.

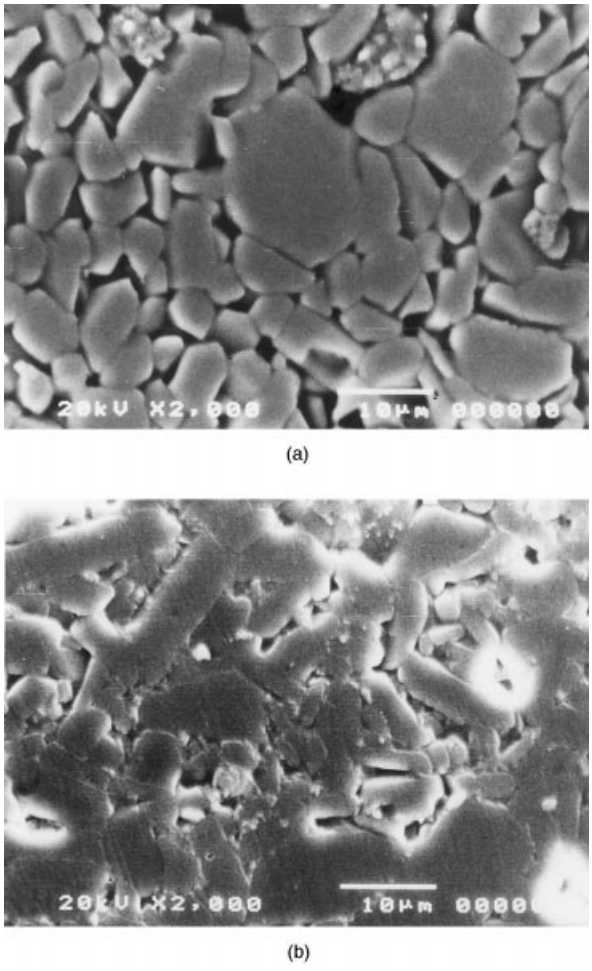

Fig. 7. Thermally etched SEM images showing the orientation and morphology in (a) tape cast and (b) slip cast specimens of $C2_S14$ sintered at 1610°C for 2 h. Note the alignment in tape casing.

and slip cast (Feret's diameter of 3.4 μm and aspect ratio of 2.1) specimens show a substantial growth of the platelets due to a higher sintering temperature and exposure time (Table 3). Higher Feret's diameter associated with a low aspect ratio in the tape cast specimen indicates a planar orientation of platelets.

3.4. Wear and mechanical properties

The wear (abrasion and erosion) loss of uniaxially pressed LPS materials derived from both coarse and medium powders with different hours of milling is seen in Table 1. Sixteen hours of milling exhibits the lowest abrasive wear loss and milling in between 12 and 16 h shows low erosive wear loss (at 45° angle of impingement). Erosion at a 90° angle of impingement does not indicate any definite trend. Table 4 represents the mechanical properties of these materials in the extruded specimens. It shows that an extended milling time hardly results in any significant improvement of flexural strength. The influence of sintering temperature and milling condition on the wear and mechanical properties of $C2_S$ composition is seen in Table 2. Wear loss is low and flexural strength is high when sintering temperature is kept low with increased sintering time (1570°C/2 h). Within the range of 14–16 h of milling, the wear results do not show a definite trend. Abrasive wear loss of $C2_S14$ materials derived from a different fabrication technique and sintered at a different temperature is presented in Table 3.

The results of Vickers hardness and fracture toughness are seen in Table 5. The fracture toughness by SENB test with $C2_Sii14$ material is found to be comparable with that of the indentation test ($K_{ic-short}$) at 9.81 N load. The $K_{ic-short}$ is higher in the case of the $C2_Si14$ material sintered in 1570°C for 1 h. The same table also shows a substantial difference in $K_{ic-short}$ due to the fabrication route in both the $A6_M16$ and $B6_I16$ materials that will be correlated with the fracture path in the later section.

Comparisons of wear loss between the auger extruded and the isopressed balls in the wet-milling test are seen

Table 4
Mechanical properties of LPS alumina milled for different hour

Material code	Flexural strength, MPa		Elastic modulus, GPa	
	$\overline{X}$	σ_{n-1}	$\overline{X}$	σ_{n-1}
$A2_M8$	269	35.2	289	3.4
$A2_M12$	288	16.2	294	1.3
$A2_M16$[a]	260	18.2	290	1.4
$A3_I4$	238	29.9	278	2.3
$A3_I12$	220	23.0	281	6.4
$A6_M16$[a]	255	28.8	310	2.1
$A6_M40$	254	34.0	317	4.4

[a] From our previous work [20].

in Table 6 for 91–97 wt% LPS materials prepared with different varieties of powders i.e. coarse, medium and reactive. Generally, the wear is low in isopressed samples except for the $B7_I16$ and $C2_S16$ materials. It, therefore, shows that the fabrication route influences the wear in a different manner depending on the material composition. An isopressed 95–97 wt% LPS Al_2O_3 prepared with 'R' powder, $H3_R16$, shows the lowest wear loss. Considering only the auger-extruded specimens, $C2_S16$, shows the lowest wear loss.

4. Discussions

4.1. Role of fabrication route and processing parameters on microstructure

Preferential orientation [3] of the particles in extrusion, tape casting or slip casting can generate an aligned microstructure in the sintered material. On the other hand, a random orientation of particles occurs in the powder compaction route and an isotropic microstructure is expected. In the present materials, the alignment of the platelets is noticed in the tape cast specimen (possibly basal plane alignment) as seen in the SEM image of Fig. 7. Seabagh et al. [4] showed aligned microstructures of seeded alumina platelets (11 μm diameter and 1.5 μm thickness) that were grown anisotropically (maximum of 25 μm diameter and 6 μm thickness) in a 5 wt% $CaO + SiO_2$ liquid medium. Crystallographically, a slower growth in the basal plane was reported. However, the present microstructure is found to be equiaxed compared to the elongated morphology reported [4]. Although the size of the platelets are similar i.e. 8–12 μm in diameter [Fig. 2(a)] and 1–2 μm in thickness [19], the microstructure is different possibly due to a different grain growth mechanism. As is known, glass with a high CaO content can induce an anisotropic grain growth whereas anisotropic growth rate is smaller in the presence of MgO [12–15]. Thus, the composition of the liquid phase in the grain boundary region can play a significant role on grain growth. The composition of the present material (4.99 SiO_2 + 0.84 CaO + 1.85 MgO, wt%) is different in respect of the MgO content compared to that of the reported material [4]. The higher MgO/(CaO + BaO + KNaO) ratio (> 1.5) in the chemical composition of the sintered material is, therefore, thought to be responsible for the differences in grain shape and size [19].

In extrusion, the non-plastic particles are reported to lie with their major cross-sectional area parallel to the surface of the extruded column [3]. Fig. 5(c) has shown

Table 5
Vickers hardness and fracture toughness of certain LPS Al_2O_3 ceramics derived from different fabrication route and sintering temperatures

Sample code	Load	d	H_v	c	l	$K_{ic-short}$		% ok	Nature of cracks
						$\overline{X}$	σ_{n-1}	crack sys.	
	N	μm	GPa	μm	μm	MPa.m$^{1/2}$			
$B6_I16^P$	24.52	64.9	10.8	75.1	42.7	3.60	0.332	100	Multiple ribbed cracks
$B6_I16^P$	49.03	91.1	11.0	112.0	65.4	3.99	0.484	100	Multiple and bridged cracks
$B6_I16$[a]	49.03	92.2	10.7	126.6	80.5	3.38	0.680	100	Zigzag and multiple cr.
$B6_I16^E$	49.03	92.7	10.6	121.6	74.9	3.56	0.491	75	Bow/straight and bridging
$A6_M16$[a]	49.03	91.6	10.9	128.1	82.3	3.33	0.613	100	Straight ribbed and multi. cr.
$A6_M16^E$	49.03	88.4	11.6	128.3	84.6	3.14	0.156	50	Zigzag, multi. and branched
$C2_Si14^P$	2.94	22.4	11.0	17.0	6.4	3.56	0.483	50	Extra cracks and bowing
	4.90	28.4	11.4	24.5	10.4	3.89	0.786	77	Bowing and extra crack
	9.81	47.6	8.5	40.9	18.1	3.71	1.087	78	Bowing and extra crack
	24.52	67.4	10.0	76.3	42.6	3.65	–	100	
$C2_Sii14^P$	4.90	29.7	10.8	32.1	17.2	2.40	0.122	100	Bowing and straight cracks
	9.81	42.4	10.2	47.0	26.8	2.75	0.455	90	Bowing/straight/zigzag cr.
	24.52	68.7	9.7	77.5	43.2	3.20	0.304	100	Multiple and ribbed cracks
(SENB)						(3.14)	(0.237)		
$C2_Sii14^E$	9.81	42.7	10.0	93.1	25.2	2.74	0.211	100	Bowing/straight/zigzag cr.
	49.03	98.6	9.4	118.3	66.0	3.38	0.111	100	Straight and multiple cracks

[a] Isopressed.

Table 6
Wear loss of the extruded and cold isopressed LPS Al_2O_3 balls

Material code	Extrusion			Isostatic pressing		
	Density g/cc	Open porosity, %	Wear loss mg/cm^2	Density g/cc	Open porosity, %	Wear loss mg/cm^2
$A1_I16$	3.59	0.05	0.428	3.56	0.05	0.374
$A2_M16$	3.68	0.01	0.425	3.69	0.04	0.278
$A6_M16$	3.70	0.03	0.372	3.71	0.05	0.355
$B6_I16$	3.66	0.08	0.391	3.72	0.01	0.264
$B7_I16$	3.60	0.10	0.241	3.59	0.21	0.332
$C2_Si14$	3.48	0.01	0.268	3.40	0.09	0.225
$C2_S16$	3.41	0.14	0.221	3.52	0.05	0.244
$A7_R16$	3.72	0.09	0.275	3.74	0.11	0.216
$H3_R16$	3.63	0.09	0.222	3.72	0.09	0.177

such a possibility of alignment in the extruded specimen of $B6_I16$. The differences observed in the elongation between the uniaxial pressing and extrusion (Figs. 3 and 4) in the plane perpendicular to the extruded column can also occur due to the planar arrangement of the platelets. In that case, a two dimensional view would constitute a thickness and a length dimension showing an apparently higher aspect ratio compared to a random orientation. This explains the high aspect ratio observed in the extruded specimens of $B7_I16$ material where grain growth anisotropy is expected to be less due to a high MgO content [19]. Based on micrographs presented above and the reported micrographs, it is observed that the fabrication route can result in a different morphology in the two dimensional images due to orientation of platelets.

When the sintering temperature is varied the grain shape and size can also change. The grains are finer and elongated when sintered at a low temperature as observed in the case of the uniaxially compacted $C2_Si14$ sintered at 1570°C/1 h [Figs. 6(a) and 8(a)]. With the rise in sintering temperature i.e. at 1600°C/1 h, grains have become thicker and coarser [4] as seen in Figs. 6(b) and 8(b). Grain size distribution (Table 7) is similar for isothermal sintering of 14 h milled ($C2_Sii14$) and 16 h milled ($C2_Svi16$) materials. Teh et al. [26] reported an incoherent relationship between the particle size distribution of the starting Al_2O_3 powder (99.99% purity) and the grain size distribution in the sintered ceramics. Table 7 also shows that the extruded $A2_M16$ has a larger grain size than that of the $A6_M16$ and the grain size of both these two materials are higher than C-type LPS materials due to a higher MgO/(CaO + BaO + KNaO) ratio [19]. Thus, the morphological changes exhibited in the present LPS materials are due to (i) fabrication

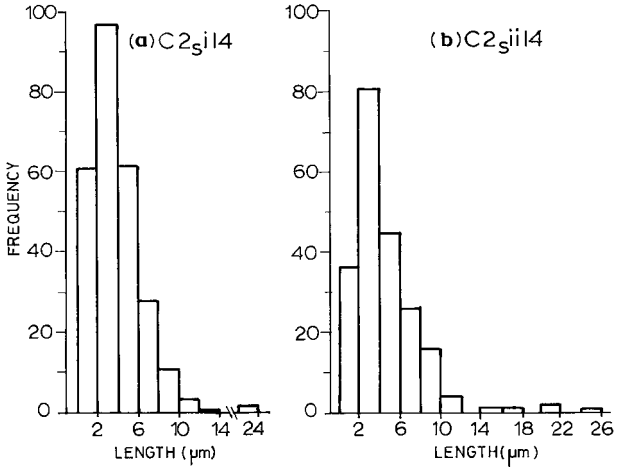

Fig. 8. Histogram showing distribution of grain length (major axis) in thermally etched $C2_S14$ materials sintered at (a) 1570°C and (b) at 1600°C both for 1 h.

Table 7
Grain size distribution, glass and pore content in certain selected LPS Al_2O_3 ceramics

	Grain size distribution (μm)								Volume % of	
	2	4	6	8	10	12	$\overline{X}$	max.	glass	pore
$A2_M16$[a]	12	20	21	11	16	20	7.6	22	21	12
$A6_M16$[a]	18	19	24	12	17	24	6.5	30	26	8
$C2_Sii14$[b]	18	43	31	5	2	2	4.7	12	22	15
$C2_Svi16$[b]	15	35	42	6	1	1	4.9	14	28	17

[a] Extruded and sintered at 1580°C/2 h.
[b] Uniaxially pressed and sintered at 1600°C/1 h.

route (ii) sintering time and temperature and (iii) impurities present in the grain boundary. The effect of particle size distribution in the milled powder on morphology shall be reported separately in our future communication.

4.2. Role of fabrication route on wear

A large difference in the wear loss between the isopressed and extruded balls has been observed in the case of $B6_I16$ (Table 6). The wear mechanisms of a polycrystalline Al_2O_3 with ~0.7% silicate impurities were investigated under a similar wear environment in aqueous media [27]. The material removal mechanisms were reported to be due to the solution of silicate materials from the grain boundary region, microfracture induced by stress corrosion cracking and dislodgment of grains. A comparison between the untested surface and wear surface in Fig. 9(a and b) reveals the dissolution of grain boundary material and dislodgment of grains in the isopressed $B6_I16$ ball. Microcracking could not be noticed in this material. On the other hand, a comparison between the untested surface and the wet-milled surfaces of extruded $A2_M16$ materials show that the material removal is associated with wear pit and extensive microcracking as seen in Fig. 10(a–c). Thus the

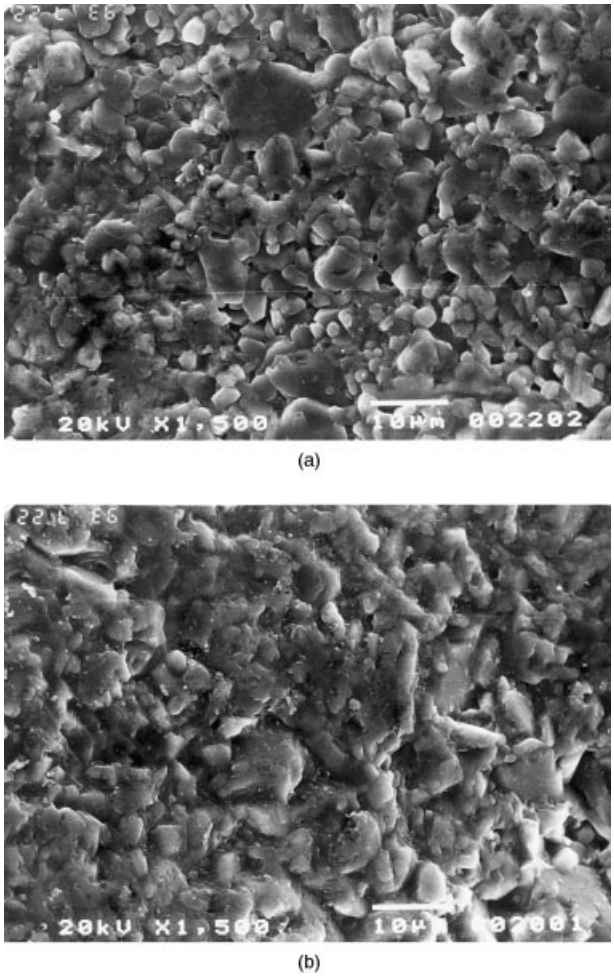

Fig. 9. SEM images of (a) untested surface and (b) wear surface of isopressed $B6_I16$ material illustrating the dissolution of grain boundary materials in the wet-milling test.

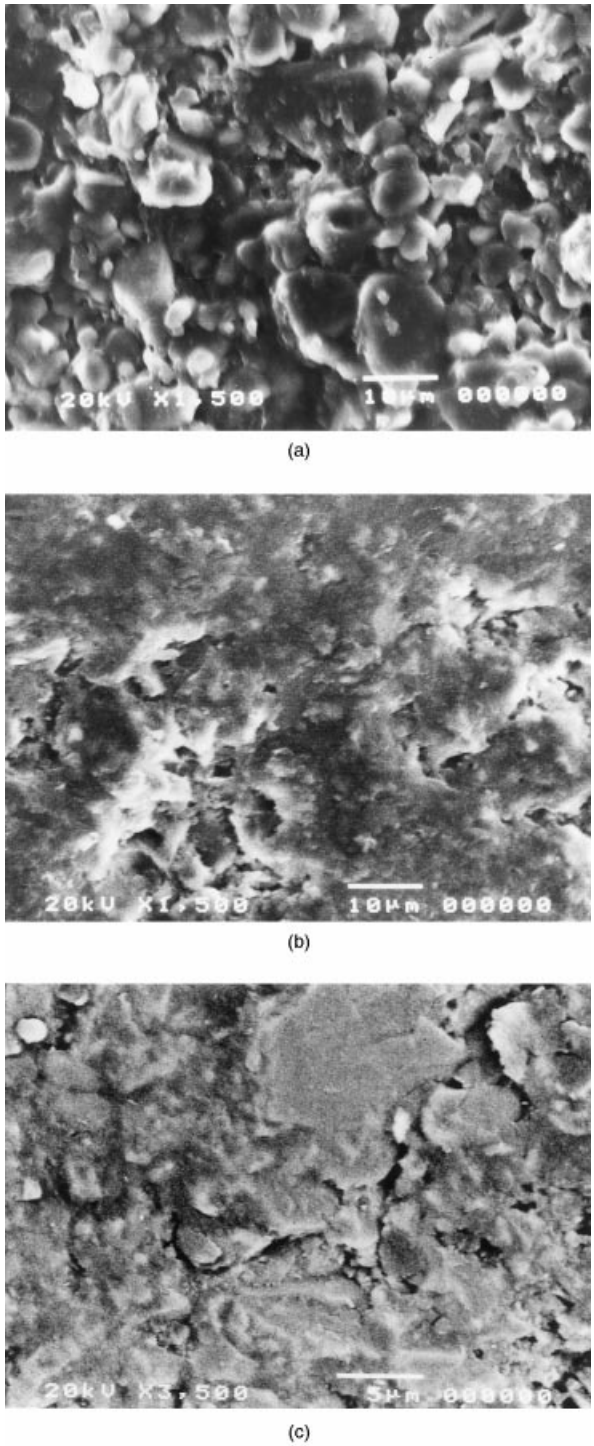

Fig. 10. SEM images of $A2_M16$ showing (a) an untested surface, and wear surfaces illustrating (b) wear pit and (c) microcracking in 'dry sand and rubber wheel' test (a and b — secondary electron and c — back scattered electron images).

extensive microcracking in the wear surface of an extruded $A2_M16$ ball is thought to be responsible for a higher wear loss in the extruded $A2_M16$ ball compared to that of the isopressed $B6_I16$.

The tape cast material always showed a high abrasive wear loss despite attaining a similar level of the theoretical density (Table 3). The SEM images of untested and wear surfaces in Fig. 11(a and b) illustrate the damage morphology in tape cast material. Microcracking and fatigue flake-like material removal is seen in the wear surface with no noticeable deformation scar. In a similar wear environment, our previous study showed that a wear surface with extensive deformation resulted in a lower material loss and a wear surface with extensive microcracking resulted in a higher loss [21]. Thus the higher wear loss in the tape cast material can possibly be explained due to the extensive microcracking. Further, the higher material removal rate of tape cast specimen can also be attributed to the planar alignment of platelets parallel to the plane of abrasion. On the other hand, the extruded specimens have low wear loss possibly due to the orientation of the platelet in a plane perpendicular to the plane of abrasion, whereas the slip cast material with a random orientation [Fig. 7(b)] shows a lower wear loss. Since both the slip cast and tape cast specimens are isothermally sintered, the influence of grain size and grain boundary composition can be assumed to be similar. It suggests that wear in an aligned microstructure may possibly be controlled by the anisotropy of the α-Al_2O_3 platelets.

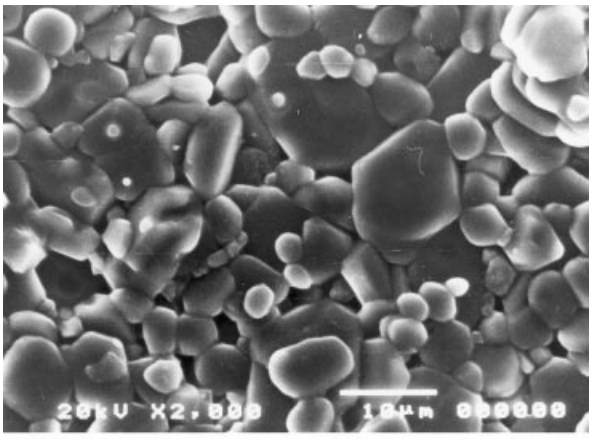

(a)

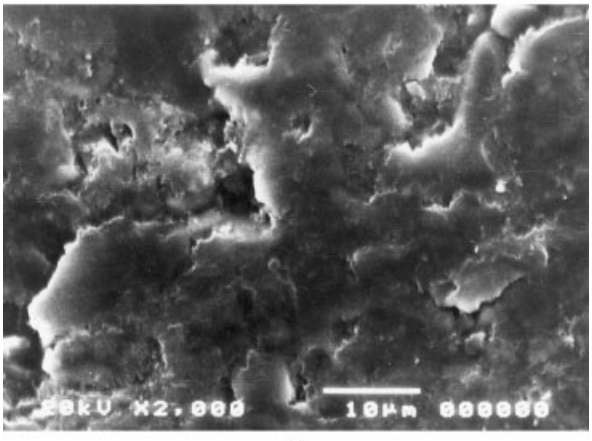

(b)

Fig. 11. SEM images of the tape cast $C2_S14$ specimen showing (a) a textured surface in the untested and (b) microcracking and fatigue-flake like material removal in wear surface after 'dry sand and rubber wheel' test.

Table 1 shows that a high density of 3.73 g/cc i.e. 97.08% of theoretical density (considering the densities of 3.98 g/cc for Al_2O_3 and 2.63 g/cc measured for the glass) has been obtained in $A6_M40$. The wear loss, however, is seen to be higher in $A6_M40$ compared to $A6_M16$. Similarly a higher density in isopressed $C2_Si14$ material does not yield a lower wear loss (Table 3). Furthermore, uniaxially pressed specimens have a low abrasive wear loss even though the density is lower (Table 2). Considering the results of all the different materials and their fabrication routes, it is found that a higher density does not always result in a lower wear loss. However, a high open porosity associated with lower density can lead to a higher wear loss. Latela et al. [28] estimated a threshold limit for the true porosity (6.8%) beyond which the erosive wear increased rapidly.

4.3. Role of fabrication route on mechanical properties

The higher $K_{ic-short}$ seen in the uniaxilly pressed $B6_I16$ can be attributed to the microstructure due to the presence of reinforcement grains in the fine-grained matrix [Fig. 5(b)]. The isopressed materials of $A6_M16$ and $B6_I16$ show a relatively lower $K_{ic-short}$ and a high variability although the latter has a relatively higher proportion of large elongated grains. Both the uniaxially pressed and extruded specimens exhibit intergranular fracture irrespective of grain size whereas the fracture path in isopressed specimens shows occurrence of some transgranular fracture as well. In our previous study with the uniaxially pressed materials of these compositions, it was reported that transgranular fracture leads to a lower toughness [20]. It was further pointed out that when the thermal expansion of the grain boundary glass was lower than Al_2O_3, a transgranular fracture occurred due to a compressive stress field in the grain boundary glass [20,29]. Hence, the residual stresses at grain boundaries caused by an unknown change in the glass could be responsible for the observed change in the fracture path associated with isopressing [21].

In the $C2_S$ composition, the mechanical properties like flexural strength and $K_{ic-short}$ have been observed to be higher in $C2_Si14$ (Tables 2 and 5). The higher $K_{ic-short}$ in $C2_Si14$ is probably due to the presence of large elongated grains of 22–24 μm length [Fig. 8(a)] in a relatively fine-grained matrix [Fig. 6(a)]. The fracture path observed is predominantly intergranular that

resulted in enhanced $K_{ic-short}$ due to crack deflection and bridging [9]. However, the variability is also higher as similarly observed by Kovar et al. [30]. A further refinement of the microstructure with regard to uniform size and distribution of reinforcement grains can be suggested for a better consistency in the $K_{ic-short}$ values. A lower $K_{ic-short}$ is observed in high temperature sintered material (Tables 2 and 5) due to coarse grains [Fig. 6(b)] and a broad grain size distribution [Fig. 8(b)]. Sintering at a higher temperature or with increased time has resulted in a higher flexural strength. Isopressing the extruded rods of $C2_S14$ (sintered at 1570°C/1 h) showed a minimized variability ($\sigma_{n-1} = 20.88$) in the flexural strength with an average of 297 MPa. Thus a higher compaction pressure may not result in stronger ceramics although it can reduce the variability by minimizing the flaws due to fabrication. A higher glass content (Table 7) in $C2_S$vi16 as a result of long milling time may be one of the factors responsible for the lower flexural strength.

5. Conclusions

Liquid-phase-sintered Al_2O_3 ceramics fabricated by different process routes e.g. slip casting, tape casting, uniaxial pressing, isopressing, piston and auger extrusion, displayed different morphologies possibly due to the orientation of platelets. In tape casting, the major face of the platelet was oriented parallel to the plane of the tape. Alignment of some of the platelets was noticed in a plane perpendicular to the direction of the extrusion in certain specimens. Slip casting and uniaxial pressing showed a random orientation.

Specimens derived from different fabrication routes showed large differences in wear loss. Tape cast specimens always showed a higher wear loss, which is thought to be due to the alignment of platelets (major face) in the plane of the test surface. Extruded specimens showed a low wear loss, possibly due to some degree of orientation perpendicular to the test surface. Randomly oriented platelets in uniaxial pressing and slip casting also showed a lower wear loss.

In the wet-milling wear test, lowest wear loss was achieved in a 95–97 wt% composition with reactive Al_2O_3 powder. A 91–94 wt% LPS of coarse powder also showed a comparable (~25% less) wear loss. Twelve to sixteen hours of batch milling was found to be beneficial for minimizing the abrasive wear loss considering both medium and coarse powders.

Sintering temperature/time was also found to have a significant influence on the grain size and shape in the microstructure. Sintering for a shorter duration (1 h) and at a lower temperature (1570°C) produced an elongated morphology with large elongated grains of 14–24 μm length in a fine-grained matrix. These large grains are thought to be responsible for enhanced indentation fracture toughness by bridging and deflection. Such a microstructure was obtained from the commercial powders by uniaxial pressing. However, as the matrix grain size was increased by raising the sintering temperature, low indentation fracture toughness was observed. Experimental results suggested that expensive powder and costly fabrication route were not essential for the production of mechanically strong and wear resistant Al_2O_3 ceramics.

Acknowledgements

Authors thank BHEL management for the necessary support. Observations by Mr. L.K. Sachdeva are gratefully acknowledged.

References

[1] S.J. Reed, Forming processes, Part VII, in: Introduction to the Principles of Ceramic Processings, John Wiley & Sons, New York, 1988, pp. 327–407.
[2] G.Y. Onoda Jr., L.L. Hench, Ceramic Processing Before Firing, John Wiley & Sons, New York, 1972.
[3] W.O. Williamson, Particle orientation in clays and whitewares and its relation to forming process, in: W.D. Kingery (Ed.), Ceramic Fabrication Process, The Technology Press of MIT, John Wiley & Sons, New York, 1958, pp. 89–98.
[4] M.M. Seabag, I.H. Kerscht, G.L. Messings, Texture development by templated grain growth in liquid-phase-sintered alumina, J. Am. Ceram. Soc. 80 (5) (1997) 1181–1188.
[5] J.L. Pentecost, C.H. Wright, Preferred orientation in ceramic materials due to forming technique, in: G.R. Mallet, M. Fay, W.M. Mueller (Eds.), Advances in X-ray Analysis, Vol. 7, Plennum Press, New York, 1964.
[6] M.J. Hanney, R. Morrell, Factors influencing the strength of a 95% alumina ceramics, in: R.W. Davidge (Ed.), Proceedings of the British Ceramic Society, Engineering with Ceramics, No. 32, British Ceramic Society, Shelton House Stoke-on-Trent, UK, 1982, pp. 277–290.
[7] J.A. Salem, J.L. Shannon, R.C. Bradt, Crack growth resistance of textured alumina, J. Am. Ceram. Soc. 72 (1) (1989) 20–27.
[8] T. Carisay, I. Levin, D.G. Brandon, Microstructure and mechanical properties of textured Al_2O_3, J. Eur. Ceram. Soc. 15 (1995) 283–299.
[9] S.J. Bennison, B.R. Lawn, Flaw tolerance in ceramics with rising crack resistance characteristics, J. Mater. Sci. 24 (1989) 3165–3169.
[10] P.F. Becher, et al., Microstructural design of silicon nitride with improved fracture toughness: II. Effects of yttria and alumina additives grain shape and size, J. Am. Ceram. Soc. 81 (1) (1998) 2831–2840.
[11] R.J. Brook, Fabrication principles for production of ceramics with superior mechanical properties, in: R.W. Davidge (Ed.), Proceedings of the British Ceramic Society, Engineering with Ceramics, No. 32, British Ceramic Society, Shelton House Stoke-on-Trent, UK, 1982, pp. 7–23.
[12] H. Song, R.L. Coble, Origin and growth kinetics of plate-like abnormal grain growth in liquid-phase-sintered alumina, J. Am. Ceram. Soc. 73 (7) (1990) 2077–2085.
[13] W.A. Kaysser, M. Sprissler, C.A. Handwerker, J.E. Bluedell, Effect of a liquid phase on morphology of grain growth in alumina, J. Am. Ceram. Soc. 70 (5) (1987) 339–343.

[14] I.J. Bae, S. Baik, Abnormal grain growth of alumina, J. Am. Ceram. Soc. 80 (5) (1997) 1149–1156.
[15] C.A. Handwerker, P.A. Morris, R.L. Coble, Effects of chemical inhomogenities on grain growth and microstructure in alumina, J. Am. Ceram. Soc. 72 (1) (1989) 130–136.
[16] D. Kolar, Discontinuous grain growth in multiphase ceramics, in: C.A. Handwerker, J.E. Blendel, W.A. Kaysser (Eds.), Ceramic Transactions, Vol. 7 Sintering of Advanced Ceramics, American Ceramic Society, Westerville, OH, 1990.
[17] E.A. Barringer, H.K. Bowen, Ceramic powder processing, Ceram. Eng. Proc. 5 (5–6) (1984) 285–297.
[18] T.J. Carbone, Production process, properties, and application for calcined and high purity aluminas, in: L.D. Hart (Ed.), Alumina Chemicals: Science and Technology Handbook, American Ceramic Society, Westerville, OH, 1990, pp. 99–108.
[19] A.P. Goswami, S. Roy, M., Mitra, G.C. Das, Impurity dependent morphology and grain growth in liquid-phase-sintered Al_2O_3, J. Am. Ceram. Soc. in press.
[20] A.P. Goswami, S. Roy, M. Mitra, G.C. Das, Microstructure dependent hardness and fracture behavior in liquid-phase-sintered Al_2O_3, Ceram. Int. 26 (4) (2000) 397–410.
[21] A.P. Goswami, S. Roy, M. Mitra, G.C. Das, Influence of powder, chemistry and microstructure on the wear resistance of liquid-phase-sintered Al_2O_3, Wear, in press.
[22] Designation: C 373-88 ASTM 1916 Race st., Philadelphia PA 19103.
[23] R.C. Bradt, et al. (Eds.), Fracture Mechanics of Ceramics, Vol 10, Plenum Press, NY, 1992, pp. 119–133.
[24] Designation: G 65 ASTM 1916 Race st., Philadelphia PA 19103.
[25] A.W. Ruff, L.K. Ives, Measurement of solid particle velocity in erosive wear, Wear 35 (1975) 195–199.
[26] T.S. Yeh, M.D. Sacks, Effect of particle size distribution on the sintering of alumina, J. Am. Ceram. Soc. 71 (2) (1988) C484–487.
[27] S. Kitaoka, Y. Yamaguchi, Y. Takahashi, Tribological characteristics of α-alumina in high temperature water, J. Am. Ceram. Soc. 75 (1992) 3075–3080.
[28] B.A. Latella, B.H. O'Connor, Effect of porosity on the erosive wear of liquid-phase-sintered alumina ceramics, J. Am. Ceram. Soc. 82 (8) (1999) 2145–2149.
[29] C.A. Powell-Dogan, A.H. Heuer, Microstructure of 96% alumina ceramic: III. Crystallization of high calcia boundary glasses, J. Am. Ceram. Soc. 73 (12) (1990) 3684–3691.
[30] D. Kovar, M.J. Ready, The role of grain size in strength variability of alumina, J. Am. Ceram. Soc. 77 (7) (1994) 1928–1938.